J Mater Sci (2009) 44:2489–2496
DOI 10.1007/s10853-009-3319-9

Preparation of mullite-based iron magnetic nanocomposite powders by reduction of solid solution

Hao Wang · Tohru Sekino · Koichi Niihara · Zhengyi Fu

Received: 18 October 2008 / Accepted: 3 February 2009 / Published online: 6 March 2009

Abstract In this article, the preparation of mullite-based iron magnetic nanocomposite powders by hydrogen reduction of Fe-doped mullite solid solution with a nominal composition of $Al_{5.4}Fe_{0.6}Si_2O_{13}$ is reported. The formation process of $Al_{5.4}Fe_{0.6}Si_2O_{13}$ solid solution was analyzed using X-ray diffraction analysis (XRD), Fourier Transform Infrared Spectrum (FT-IR), thermogravimetric, and differential thermal analysis (TG-DTA). It is found that doping with Fe^{3+} cation affects the crystallization temperature of mullite. During the hydrogen reduction process, more than 89% Fe^{3+} cation in solid solution were transformed into α-Fe phase when reduction temperature reached 1200 °C. Microstructure characterization of nanocomposite powders reduced at 1300 °C reveals that there are two types of α-Fe particles in mullite matrix. Fe nanoparticles with a size of approximately 10 nm were precipitated within the mullite grains, while Fe particles larger than hundreds of nanometers were located at the surfaces of the mullite grains. The measurement of the magnetic properties of nanocomposite powders indicates that large particles and nanoparticles of α-iron have the ferromagnetic and superparamagnetic behavior at room temperature, respectively.

H. Wang (✉) · Z. Fu
State Key Lab of Advanced Technology for Materials Synthesis and Processing, Wuhan University of Technology, 122 Luoshi Road, Wuhan 430070, People's Republic of China
e-mail: shswangh@whut.edu.cn

T. Sekino
The Institute of Multidisciplinary Research for Advanced Materials, Tohoku University, 2-1-1 Katahira, Aoba-ku, Sendai 980-8577, Japan

K. Niihara
Extreme Energy-Density Research Institute, Nagaoka University of Technology, 1603-1 Kamitomioka, Nagaoka, Niigata 940-2188, Japan

Introduction

Nanocomposite powders with well-dispersed metal nanoparticles in oxide ceramic matrixes have attracted great research interests owing to their unique magnetic, optical, electrical, optoelectronic, and catalytic properties [1–5]. Various techniques, such as the mechanical mixing of powders [6, 7], mechanosynthesis [8, 9], vapor deposition [10], chemical vapor condensation [11], hydrothermal precipitation [12], sol–gel method [13, 14], spray pyrolysis [15] etc., have been employed to prepare nanocomposite powders. In particular, the reduction of metal oxide precursors in hydrogen has been commonly used in the preparation process. Following the novel concept of the ceramic-based nanocomposites for structural and multifunctional applications [16], a series of metal/ceramic nanocomposites, such as Al_2O_3/Ni, Al_2O_3/Mo, ZrO_2/Mo, ZrO_2/Ni, MgO/Fe, etc., were fabricated by reducing and hot pressing the mixtures of oxide ceramics and metal oxide powders [6, 17–20]. The microstructure evolution of metal/ceramic nanocomposites in different processing stage has been thoroughly studied, such as in Al_2O_3/Ni system [17]. It is found that fine nickel particles with narrow particle-size distribution around 30 nm precipitated uniformly around Al_2O_3 particles after reduction process. After hot pressing, most of Ni particles with an average size of about 130 nm were located at the grain boundaries and/or the triple point junctions of Al_2O_3 matrixes in dense nanocompites. The rest of Ni particles were dispersed within the Al_2O_3 matrix grains with an average size of

49 nm. It is supposed that the small nickel particles that existed at the triple points were trapped in the grains during matrix grain growth in an early stage of sintering [17]. No evidence that directly demonstrates the precipitation of Ni nanoparticles inside Al_2O_3 particles during reduction process has been reported.

In the case that metal nanoparticles are only dispersed around oxide ceramic particles, it is difficult to avoid oxidation of metal nanoparticles once nanocomposite powders are exposed to oxidation atmosphere. In contrast, it is possible to overcome this weakness by uniformly precipitating metal nanoparticles inside ceramic particles. Based on selective reduction of metal cations in homogenous metal oxide solid solutions, Rousset et al. [21–24] developed a method to prepare metal/ceramic nanocomposite powders from Al_2O_3, MgO, Cr_2O_3, and spinel solid solutions. These oxide solid solutions were normally obtained from mixed oxalate precursors after heat treatment. In these nanocomposite powders, a portion of metal nanoparticles with the size less than tens of nanometers were precipitated inside the oxide ceramic particles. However, the preparation and selective reduction of other oxide solid solutions with different synthesis routes have not been sufficiently studied.

As the only stable crystalline phase at atmospheric pressure in the aluminosilicate (Al_2O_3–SiO_2) system, mullite is widely investigated for high-temperature structural, electrical, and optical applications [25]. Besides the replacement of Si^{4+} and Al^{3+} that lead to form non-stoichiometric compound, mullite can also incorporate different amounts of transition metal cations by substituting Al^{3+} ion at different positions [26]. Since the formation of solid solution can strongly affect the physical properties of mullite, extensive studies have been carried out [27–31]. In the case of Fe-doped mullite, 12 wt% Fe_2O_3 can be dissolved in mullite matrix at 1200 °C [32, 33]. By traditional ceramic method [34], sol–gel method [35], pyrolysis of aerosols [36], etc., the Fe-doped mullite solid solution has been successfully synthesized. However, the research of mullite-based iron nanocomposite powders prepared by reduction of solid solution is limited so far.

Compared with magnetite or ferrite, iron nanoparticles are very important magnetic materials for their strong magnetism, which are practically applied in catalysis, magnetic recording, magnetic fluids, biomedicine, etc. [37–39]. It is well-known that their magnetic properties strongly depend on particle size and their arrangement of nanoparticles [40]. In the metal/ceramic nanocomposite powders prepared from reduction of solid solution, a bimodal size distribution of metal nanoparticles corresponding to different locations is normally formed [23, 24]. For this reason, it is interesting to investigate the magnetic properties of iron nanoparticles with different particle sizes obtained by reducing Fe-doped mullite solid solution.

In this article, we described the synthesis process of mullite-based iron nanocomposite powders prepared by hydrogen reduction of sol–gel made Fe-doped mullite solid solution powders. With a nominal composition of $Al_{5.4}Fe_{0.6}Si_2O_{13}$, the formation process and microstructure of Fe-doped mullite and iron nanoparticles dispersed nanocomposite powders were studied. The magnetic behavior of mullite-based iron nanocomposite powders at room temperature and 10 K were also investigated.

Experimental procedure

Preparation of materials

To synthesize Fe-doped mullite solid solution with a nominal composition of $Al_{5.4}Fe_{0.6}Si_2O_{13}$, aluminium nitrate ($Al(NO_3)_3 \cdot 9H_2O$; High Purity Chemicals, 99.9%), iron nitrate ($Fe(NO_3)_3 \cdot 9H_2O$; High Purity Chemicals, 99.9%) and tetraethyl orthosilicate (TEOS, $Si(OC_2H_5)_4$; Wako, 95%) were used as the precursors for alumina, iron oxide, and silica, respectively. After dissolving $Al(NO_3)_3 \cdot 9H_2O$ and $Fe(NO_3)_3 \cdot 9H_2O$ together with ethanol (nitrate/ethanol molar ratio equals 1:12), the solution was stirred and refluxed at 60 °C for 12 h and then $Si(OC_2H_5)_4$ (previously mixed with ethanol at TEOS/ethanol molar ratio of 1:4) was added dropwise. The solution was continuously stirred for another 12 h whereafter adjusting its pH value to 7 by slowly adding ammonia (Wako, 28%) to form gel. The gel was washed for several times by ethanol and dried in a rotary evaporator at 60 °C. In order to eliminate organics, dried gel powders were heated to 500 °C in air for 2 h at a heating rate of 10 °C/min. Powders were further calcinated at increasing temperature from 500 °C to 1300 °C for 4 h in air to study the formation process of Fe-doped mullite solid solution. The sample, which was calcinated at 1200 °C in air for 4 h, was reduced by pure hydrogen at a flowing rate of 50 ml/min to obtain the mullite-based iron magnetic nanocomposite powders. The reduction process was conducted in a multi-purpose high-temperature furnace (Hi-multi 5000, Fuji Denpa Co. Ltd., Japan) at a heating rate of 20 °C/min between 1000 °C and 1400 °C for 1 h.

Characterization

The thermal behavior of dried gel powders was monitored using TG-DTA (TG-DTA 2020SAF, Bruker Axs Co. Ltd., UK) in air at a heating rate of 10 °C/min. The FT-IR Spectra (FT-IR Spectrometer Spectrum 2000, Perkin Elmer, USA) of powders calcinated at different temperature were recorded from 400 to 1300 cm^{-1} with the samples diluted in

KBr. The crystalline phases of powders were recorded between 10° and 90° at a rate of 4° 2θ/min by XRD (RU-200B, Rigaku Co. Ltd., Japan) using Cu Kα radiation. The powder XRD patterns for lattice parameters calculation and XRD quantitive analysis were measured at a rate of 0.5° 2θ/min with silicon as an internal standard. Diffraction peaks were indexed with the PowderX package [41]. Lattice parameters were calculated with the Chekcell program [42]. The mass contents of Fe phase in final materials were determined by means of reference intensity ratios (RIR) method using Materials Data Inc. (MDI) Jade 5 software. The bright field (BF) micrographs of powders before and after reduction at 1300 °C were observed by transmission electron microscope (TEM; H-8000T, Hitachi Co. Ltd., Japan) operating at 200 kV. The sample was dispersed in ethanol and dropped on a carbon-coated copper grid. The composition of nanocomposite powders was determined by TEM energy dispersive X-ray (EDX) microanalysis. The magnetic properties of sample reduced at 1300 °C were measured by Quantum Design MPMS superconducting quantum interference device (SQUID) magnetometer. Static magnetizations were obtained at 10 and 300 K with magnetic field up to 10 kOe. Zero-field-cooled (ZFC) magnetizations were recorded by cooling sample in a zero magnetic field to 10 K and then by increasing the temperature to 300 K in an applied field of 100 Oe, while field-cooled (FC) magnetizations were measured by cooling the sample from 300 to 10 K in the same field of 100 Oe.

Results and discussion

Fe-doped mullite solid solution

The TG-DTA curve of Fe-doped mullite precursors is presented in Fig. 1. The endothermal peaks at 54 and 127 °C are corresponding to the evaporation of ethanol and water left in dried gel powders, respectively. The large exothermal peak around 264 °C is generated by the exothermic decomposition of ammonium nitrate in the diphasic gel [43]. Along with the removal of volatile impurity, the weight of powders is quickly declined with increasing temperature till 400 °C. The other exothermal peak appears at 950 °C, which is related to the crystallization of amorphous phases.

XRD patterns of powders after heat treatment at different temperature are shown in Fig. 2. Amorphous powders without volatile impurities were obtained after heat treated at 500 °C. The powders remained amorphous with the appearance of some very weak diffraction peaks of $Al_3Fe_5O_{12}$ at 800 °C. As the calcination temperature reached 1000 °C, a great deal of crystallized $Al_3Fe_5O_{12}$ and poor-crystallized γ-Al_2O_3 were formed, meanwhile the

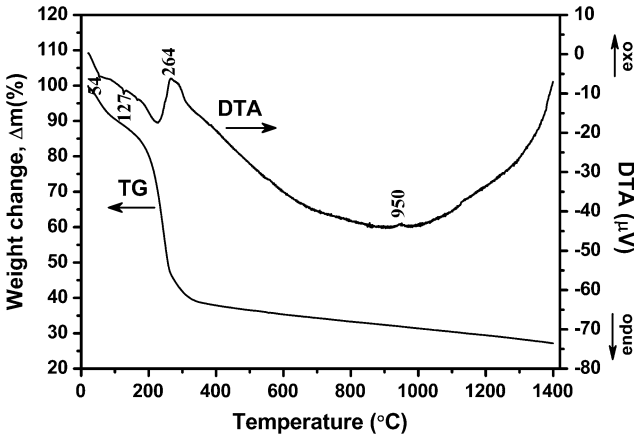

Fig. 1 TG-DTA curve of Fe-doped mullite solid solution precursors

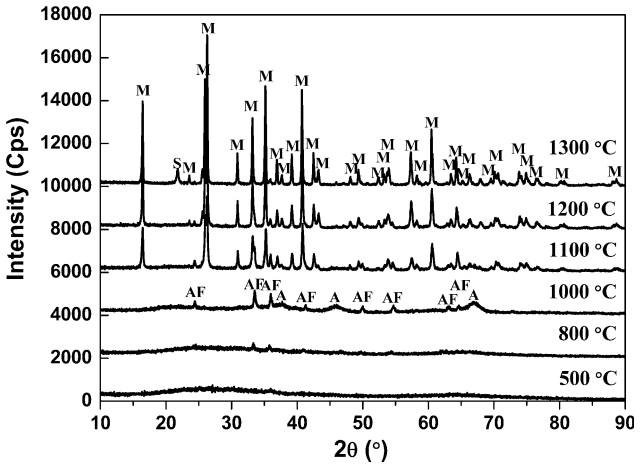

Fig. 2 XRD profiles of dried gel powders calcinated at various temperatures. *M* Fe-doped mullite solid solution, *S* cristobalite, *A* γ-Al_2O_3, and *AF* $Al_3Fe_5O_{12}$

silica was still in amorphous state. The crystallization process was also detected by forming exothermal peak at 950 °C in DTA curve (see Fig. 1). After calcinated at 1100 °C, the pseudo-tetragonal mullite was formed by the reaction of $Al_3Fe_5O_{12}$, γ-Al_2O_3, and amorphous silica. There is no significant difference in the XRD patterns between the samples calcinated at 1200 and 1300 °C, except the appearance of a small diffraction peak of cristobalite in the sample obtained at higher calcination temperature. Orthorhombic mullite solid solution with the complete dissolution of Fe^{3+} cation was formed after heat treated at 1200 °C. Compared with pure mullite prepared by the same method [44], the temperature of mullitization was decreased for about 150 °C by the dissolution of Fe^{3+} cation.

The structure evolution of Fe-doped mullite solid solution at different calcination temperature was monitored by FT-IR spectra (see Fig. 3). The spectra of the samples

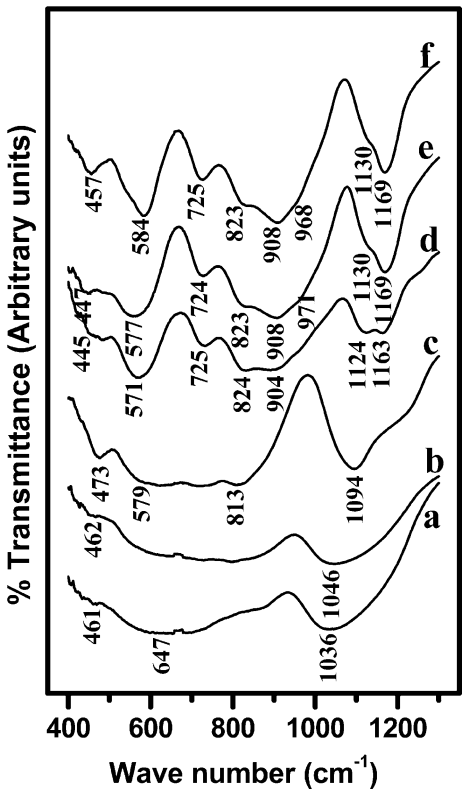

Fig. 3 The FT-IR spectra of dried gel powders calcinated at different temperature. (a) 500 °C, (b) 800 °C, (c) 1000 °C, (d) 1100 °C, (e) 1200 °C, and (f) 1300 °C

calcinated at 500 and 800 °C are similar, showing a very broad band without much fine structure in 400–900 cm^{-1} and an intense broad band around 1040 cm^{-1}. The broad band observed around 1040 cm^{-1} is assigned to the anti-symmetric stretching vibrations of the Si–O–Si in amorphous silica and Si–O–Al networks [44]. The absence of fine structure in the 400–900 cm^{-1} region is probably due to the existence of nanostructured Al_2O_3, Fe_2O_3, SiO_2, and Al_2O_3–SiO_2 agglomeration in the amorphous state [44].

With the increase of the calcination temperature up to 1000 °C, two peaks and one broad band were observed. The sharp peaks at 473 and 1094 cm^{-1} are assigned to the stretching and bending vibration of SiO4, respectively. The broad band from 579 to 813 cm^{-1} covers the vibration modes of tetrahedrally coordinated Al–O bond and octahedrally coordinated Al–O and Fe–O bonds [44, 45]. The tetrahedron and octahedron seem to be highly disordered since the wave number occupies a wide range. The presence of both tetrahedrally and octahedrally coordinated Al–O bonds reveals a combination between Al_2O_3 and SiO_2 [44]. The stepwise shift of Si–O bands toward high wave numbers also indicates the formation of γ-Al_2O_3 containing a small amount of SiO_2 [46]. This phenomenon is coincident with the result of XRD patterns (see Fig. 2). After heat treated at 1100 °C, pseudo-tetragonal mullite has been already formed with appearance of the characteristic peaks at 1124 and 1163 cm^{-1}. These peaks are correspondent to the stretching vibrations of Si–O–Si in SiO4 and Si–O–Al, respectively. As the transformation from pseudo-tetragonal to orthorhombic mullite at 1200 °C, more Si–O–Al bonds were formed, which result in the peak at 1124 cm^{-1} turning to a shoulder [47]. The spectra of samples calcinated at 1200 and 1300 °C are quite similar. It shows that the formation of orthorhombic mullite has been completed at around 1200 °C. It is noteworthy that bands at 445 and 571 cm^{-1} in the sample calcinated at 1100 °C gradually shifted toward high wave numbers with the increase of calcination temperature. In the FT-IR spectrum of pure mullite, bands locating around 420 and 570 cm^{-1} are assigned to the octahedrally coordinated Al–O bond [44]. It is known that the Al^{3+} cation is mainly replaced by Fe^{3+} cation at octahedral position in Fe-doped mullite [35, 36]. The substitution varies the strength and length of octahedrally coordinated Al–O bond to some extent, which may result in the shift of bands around 420 and 570 cm^{-1}.

Nanocomposite powders

Figure 4 shows the XRD patterns of samples reduced at 1000–1400 °C by hydrogen flow. Besides a small quantity of cristobalite in some samples, the mullite and α-Fe are the only two phases detected in all the samples. Since the Fe^{3+} cation locates on the lattice of mullite, high reduction temperature is essential to supply enough reductive ability to obtain the metal phase, which is quite different from that of metal oxides mixture (around 700 °C [17]). Only Fe^{3+} cation can be reduced from the Fe-doped mullite because of its lowest stability among the metal cations in solid solution under this reduction condition. The precipitation of iron phase from the lattice of Fe-doped mullite solid

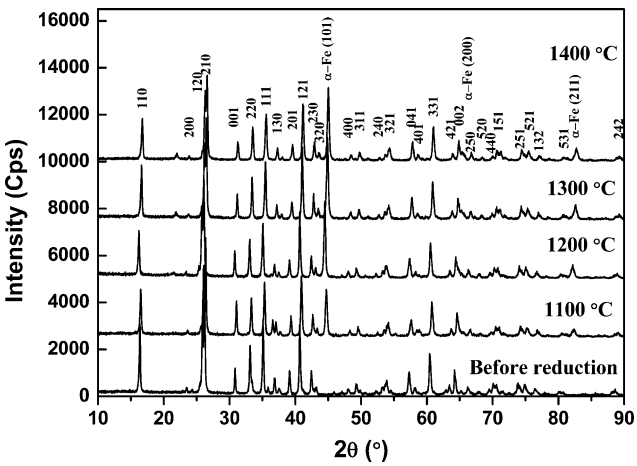

Fig. 4 XRD profiles of Fe-doped mullite solid solution powders before and after reduction in hydrogen flow at various temperatures

Table 1 Summary of the crystallographic parameters of mullite and iron phases, as well as the mass content of iron phase in the samples reduced at different temperature

Reduction temperature (°C)	Mullite, a (Å)	Mullite, b (Å)	Mullite, c (Å)	Volume of mullite's unit cell (Å^3)	Fe, a (Å)	Mass content of Fe (wt%)
Before reduction	7.5757 (35)	7.7177 (44)	2.9021 (19)	169.678	–	–
1000	7.5472 (17)	7.6962 (18)	2.8873 (8)	167.710	2.8702 (1)	2.81
1100	7.5437 (11)	7.6926 (13)	2.8847 (4)	167.402	2.8702 (12)	4.96
1200	7.5439 (13)	7.6898 (12)	2.8837 (4)	167.287	2.8670 (5)	6.94
1300	7.5413 (14)	7.6909 (13)	2.8842 (5)	167.283	2.8635 (2)	7.22
1400	7.5419 (12)	7.6909 (13)	2.8840 (5)	167.284	2.8621 (1)	7.29

solution results in the decrease of lattice parameters and volume of unit cell of mullite crystal. The crystallographic parameters of mullite and iron phases as well as the mass content of iron phase in the samples reduced at different temperature are summarized in Table 1. The lattice parameters and volume of unit cell of mullite sharply decline with the increase of reduction temperature till 1200 °C and then stay without significant changes. It reveals that the Fe^{3+} cation has been almost completely transformed into iron phase when the reduction temperature is higher than 1200 °C. The variation of mass content of iron phase in nanocomposite powders with reduction temperature shows the same tendency. Considering the theoretical mass content of iron (7.81 wt%) in nanocomposite powders after full reduction of $Al_{5.4}Fe_{0.6}Si_2O_{13}$, it shows that more than 89% and 93% Fe^{3+} cation have been reduced to α-Fe phase at 1200 and 1300 °C. The lattice parameter of α-Fe phase continuously decreases with the increase of reduction temperature, which implies that both the degree of crystallization and the microstrain in α-Fe particles may probably increase.

Figure 5 shows the TEM bright field micrographs of mullite-based iron nanocomposite powders before and after reduction in hydrogen. Fe-doped mullite solid solution particles (see Fig. 5a), with the grain size around 100 nm, have homogenous microstructure without the presence of secondary phase. On the contrary, two kinds of dark particles with different particle sizes were observed in the sample reduced at 1300 °C (see Fig. 5b and e). The dark particles with the size larger than 200 nm can be determined as α-Fe grains by EDX spectrum (shown in Fig. 5c). During the reduction process, fine iron particles among mullite grains will be firstly formed from the reduction of Fe^{3+} cation located at and near the surface of the mullite solid solution grains. Similar to the situation in the mixture of metal and ceramic particles, ceramic particles can hardly prevent these fine iron particles from agglomerating and growing with the increase of reduction temperature. In contrast, the Fe^{3+} cation located inside mullite grains will be reduced subsequently at the reduction temperature higher than 1000 °C, which leads to the formation of α-Fe nanoparticles uniformly embedded within mullite grain (see Fig. 5e). Because α-Fe nanoparticles inside mullite grain are separated from each other, the agglomeration and grain growth need to overcome the extra diffusion barrier created by mullite crystal. It can hardly distinguish the signal of Fe element in the EDX spectrum of mullite matrix (shown in Fig. 5d), which results from both the well-dispersion and relatively low content of iron phase inside mullite grain. From Fig. 5e, the α-Fe nanoparticles embedded in the mullite grain show Moiré fringe patterns. This is an indication that the certain planes of two different crystallites, as the embedded α-Fe nanoparticles and the mullite grain matrix, having a slight lattice mismatch are superimposed [48]. It is worth noting that the Moiré fringe patterns of all embedded α-Fe nanoparticles are almost the same. The actual formation mechanism of the same Moiré fringe patterns in one mullite grain has not been clarified yet. In Fe-doped mullite solid solution, Fe^{3+} cation are mainly located in octahedral position, which shows the possibility of Fe^{3+} cation emerging in ordered positions in the mullite lattice. We suppose that the embedded α-Fe nanoparticles succeeded the ordered structure of Fe^{3+} cation from Fe-doped mullite solid solution after reduction, and exhibited the specific orientation relationship of the certain planes between α-Fe and mullite crystallites. Additional study is now under investigation using high resolution TEM.

Magnetic behavior of nanocomposite powders

Figure 6 shows the magnetic hysteresis loops for mullite-based iron nanocomposite powders measured at temperature of 10 K (see Fig. 6a) and 300 K (see Fig. 6b). Saturated magnetizations (Ms), remanence ratio (Mr/Ms), and coercivity (Hc) of nanocomposite powders are 14.81 emu/g, 0.72%, 15 Oe at 300 K and 15.78 emu/g, 1.49%, 38 Oe at 10 K, respectively. Compared with the magnetic properties reported in iron oxide/mullite nanocomposite with a nominal composition of $Fe_1Al_5Si_2O_{13}$ [49], much higher Ms and much lower Hc were recorded. Correcting for the composition of nanocomposite powders,

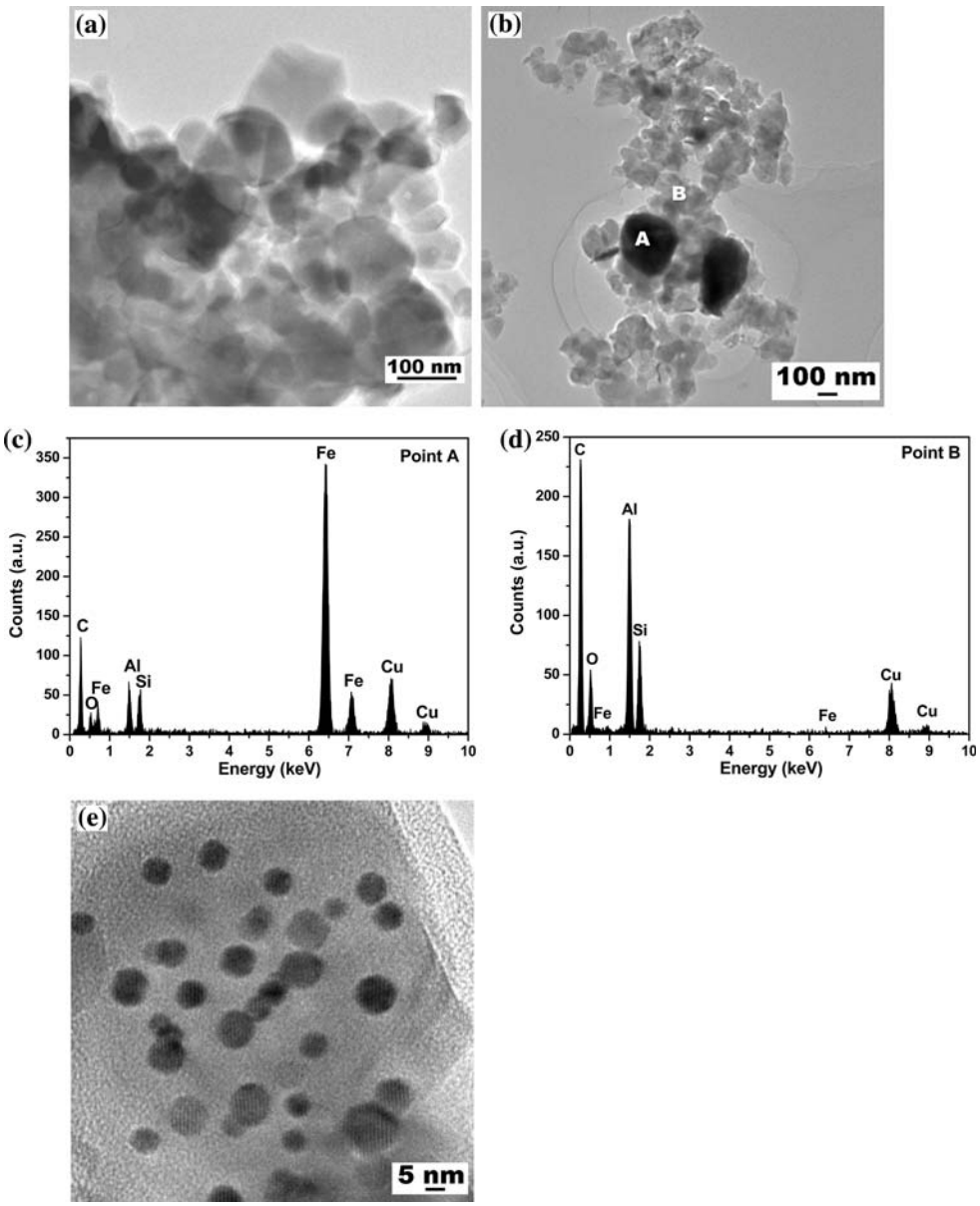

Fig. 5 The TEM bright field micrographs of powders before and after reduction at 1300 °C in hydrogen flow. **a** Before reduction, Fe-doped mullite solid solution, **b** after reduction at 1300 °C, iron grains among mullite grains, **c** EDX spectrum of point A in **b**, **d** EDX spectrum of point B in **b**, **e** reduction at 1300 °C, iron nanoparticles within mullite grain

7.22 wt% of Fe as determined from XRD quantitative analysis, the Ms is 205 emu/(gram of Fe) at 300 K, close to the expected saturation moment of 213 emu/g for bulk Fe. It is evident that the α-Fe grains with the particle size large than 200 nm should show the ferromagnetic behavior at room temperature.

It is known that for a superparamagnetic particle system, both coercive field and remnant magnetization increase with the decrease of temperature below the ferromagnetic–superparamagnetic transition temperature. This increase is due to the lower thermal activation energy of spins at low temperature [50]. In our results, the change of Hc and Mr/Ms with temperature implies the existence of superparamagnetic iron nanoparticles in mullite-based iron nanocomposite powders. In magnetism, the temperature dependence of the magnetization for nano-sized magnetic particles reveals typical characteristic of superparamagnetism, showing the blocking temperature (T_B) at which the zero-field-cooled magnetization curve exhibits a cusp [51]. Figure 7 shows the result of magnetization versus temperature for field-cooled and zero-field-cooled experiments. It is found that a maximum appears at around 100 K in the zero-field-cooled curve, which is corresponding to the blocking temperature. However, the zero-field-cooled and field-cooled magnetization curves do not completely overlap with each other above 100 K, which indicates the existence of ferromagnetic particles. As known, the magnetic behavior of metal nanoparticles is tightly related with their particle size. In the case of iron nanoparticles, the critical size of superparamagnetism is 14 nm [52]. From the observation of TEM,

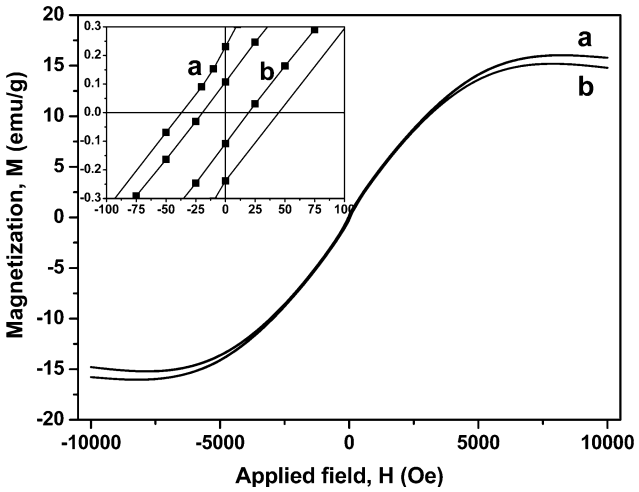

Fig. 6 The hysteresis loops for mullite-based iron magnetic nanocomposite powders measured at different temperature. Insert shows enlargement of the plot near the origin. (*a*) At 10 K, (*b*) at 300 K

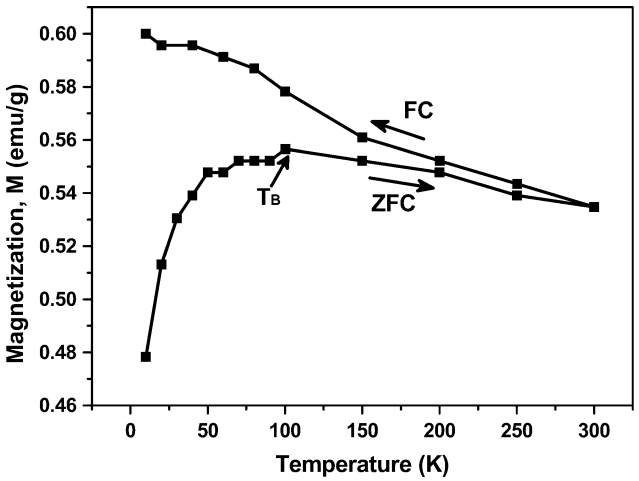

Fig. 7 The field-cooled and zero-field-cooled curves of mullite-based iron magnetic nanocomposite powders reduced at 1300 °C in an applied field of 100 Oe

most of the iron nanoparticles within mullite grains are less than the critical size, which should show the superparamagnetic behavior at room temperature. In the meantime, α-Fe grains larger than hundreds of nanometers among mullite grains are in the state of ferromagnetism.

Conclusion

The Fe-doped mullite solid solution was obtained through the heat treatment of sol–gel made amorphous gel powders. Compared with the synthesis of pure mullite, the temperature of mullitization in Fe-doped mullite is decreased for about 150 °C by the dissolution of Fe^{3+} cation. Mullite-based iron nanocomposite powders were prepared by hydrogen reduction of Fe-doped mullite solid solution. Temperature higher than 1000 °C is essential to reduce the Fe^{3+} cation inside mullite grain. More than 89% of all Fe^{3+} cation, normalized by theoretical mass content of iron in nanocomposite powders, were transformed into α-Fe phase when the reduction temperature exceeded 1200 °C. Two types of α-Fe particles, the grains larger than hundreds of nanometers among mullite grains and nanoparticles around 10 nm embedded in the grains of mullite were formed after reduction at 1300 °C. The measurement of magnetic properties of nanocomposite powders suggests that the α-Fe grains and embedded nanoparticles have the ferromagnetic and superparamagnetic behavior at room temperature, respectively. The blocking temperature of α-Fe nanoparticles within mullite grain is about 100 K.

Acknowledgements H. Wang acknowledges the financial support form the program for New Century Excellent Talents in University (NCET-05-0658) and the Scientific Research Foundation for the Returned Overseas Chinese Scholars, State Education Ministry and A3 Foresight Program from Natural Science Foundation of China (NSFC No. 50821140308).

References

1. Corrias A, Casula MF, Falqui A, Paschina G (2004) Chem Mater 3130:16
2. Epifani M, Giannini C, Tapfer L, Vasanelli L (2000) J Am Ceram Soc 2385:83
3. Oldfield G, Ung T, Mulvaney P (2000) Adv Mater 1519:12
4. Zeng HB, Cai WP, Li Y, Hu JL, Liu PS (2005) J Phys Chem B 18260:109
5. Venezia AM, Pantaleo G, Longo A, Di Carlo G, Casaletto MP, Liotta FL, Deganello G (2005) J Phys Chem B 2821:109
6. Nawa M, Sekino T, Niihara K (1994) J Mater Sci 29:3185. doi: 10.1007/BF00356661
7. Ambrose T, Gavrin A, Chien CL (1992) J Magn Magn Mater L311:116
8. Li JG, Ni X, Wang G (2007) J Alloys Compd 349:440
9. Liu KW, Mücklich F (2003) Script Mater 207:49
10. Wan Q, Lin CL, Zhang NL, Liu WL, Yang G, Wang TH (2003) Appl Phys Lett 3162:82
11. Kim JC, Lee JW, Park BY, Choi CJ (2008) J Alloys Compd 258:449
12. Shang Y, Weert GV (1993) Hydrometallurgy 273:33
13. Santos A, Ardisson JD, Tambourgi EB, Macedo AAA (1998) J Magn Magn Mater 247:177–181
14. Rodeghiero ED, Tse OK, Chisaki J, Giannelis EP (1995) Mater Sci Eng A 151:195
15. Choa YH, Yang JK, Kim BH, Jeong YK, Lee JS, Nakayama T, Sekino T, Niihara K (2003) J Magn Magn Mater 12:266
16. Niihara K (1991) J Ceram Soc Jpn 974:99
17. Sekino T, Nakajima T, Ueda S, Niihara K (1997) J Am Ceram Soc 1139:80
18. Nawa M, Yamazaki K, Sekino T, Niihara K (1994) Mater Lett 299:20
19. Kondo H, Sekino T, Choa YH, Kusunose T et al (2002) J Nanosci Nanotechnol 485:2
20. Nakayama T, Kim BS, Kondo H et al (2004) J Euro Ceram Soc 259:24

21. Laurent Ch, Rousset A, Verelst M, Kannan KR, Raju AR, Rao CNR (1993) J Mater Chem 513:3
22. Laurent Ch, Blaszczyk Ch, Brieu M, Rousset A (1995) Nanostruct Mater 317:6
23. Carles V, Laurent Ch, Brieu M, Rousset A (1999) J Mater Chem 1003:9
24. Quénard O, Grave ED, Laurent Ch, Rousset A (1997) J Mater Chem 2457:7
25. Aksay IA, Dabbs DM, Sarikaya M (1991) J Am Ceram Soc 2343:74
26. Parmentier J, Vilminot S (1998) J Alloys Compd 136:264
27. Schneider H (1986) N Jb Min Mh 172:49
28. Schneider H (1984) J Am Ceram Soc C130:67
29. Ford WE, Rees WJ (1946) Trans Brit Ceram Soc 125:45
30. Baudin C, Osendi MI, Moya JS (1983) J Mater Sci Lett 186:2
31. Schneider H (1987) J Am Ceram Soc 43:70
32. Murthy MK, Hummel FA (1960) J Am Ceram Soc 267:43
33. Chaudhuri SP, Patra SK (2000) J Mater Sci Lett 4735:35
34. Brownell WE (1958) J Am Ceram Soc 226:41
35. Berry FJ, Bilsborrow RL, Dent AJ, Mortimer M, Ponton CB, Purser BJ, Whittle KR (1999) Polyhedron 1083:18
36. Ocaña M, Caballero A, González-Carreño T, Serna CJ (2000) Mater Res Bull 775:35
37. Sun S, Andres S, Hamann HF, Tiele JU, Baglin JEE, Thomson T, Fullerton EE, Murray CB, Terris BD (2002) J Am Chem Soc 2884:124
38. Huber D (2005) Small 482:1
39. Matsumoto M, Miyata Y (2002) J Appl Phys 9635:91
40. Tartaj P, González-Carreño T, Bomatí-Miguel O, Serna CJ (2004) Phys Rev B 094401:69
41. Dong C (1999) J Appl Cryst 838:32
42. Laugier J, Bochu B (2001) Chekcell Graphical Powder Indexing Cell and Space group Assignment Software, http://www.inpg.fr/LMGP. Accessed 16 Oct 2003
43. Skordilis CS, Pomonis PJ (1993) Thermochim Acta 137:216
44. Padmaja P, Anilkumar GM, Mukundan P, Aruldhas G, Warrier KGK (2001) Inter J Inorg Mater 693:3
45. Šarić A, Musić S, Nomura K, Popović S (1998) Mater Sci Eng B 43:56
46. Jin XH, Gao L, Guo JK (2002) J Euro Ceram Soc 1307:22
47. Voll D, Angere P, Beran A, Schneider H (2002) Vib Spectrosc 237:30
48. Pana O, Teodorescu CM, Chauvet O, Payen C, Macovei D, Turcu R, Soran ML, Aldea N, Barbu L (2007) Surf Sci 4352:601
49. Morales MP, González-Carreño T, Ocaña M, Alonso-Sañudo M, Serna CJ (2000) J Solid State Chem 458:155
50. Wilson JL, Poddar P, Fray NA, Srikanth H, Mohomed K, Harmon JP, Kotha S, Wachsmuth J (2004) J Appl Phys 1439:95
51. Yoon M, Kim YM, Kim Y, Volkov V, Song HJ, Park YJ, Vasilyak SL, Park IW (2003) J Magn Magn Mater 357:265
52. Löffler JF, Meier JP, Doudin B, Ansermet JP, Wagner W (1998) Phys Rev B 2915:57